UNIVERSITY OF
BATH

University of Bath

Alternative formats
If you require this document in an alternative format, please contact:
openaccess@bath.ac.uk

Eigenstrain Boundary Layer Modelling of the Yttria-Partially Stabilised Zirconia – Porcelain Interface in Dental Prostheses

Alexander J. G. Lunt[a][*] (a.j.g.lunt@bath.ac.uk) & Alexander M. Korsunsky[b] (alexander.korsunsky@eng.ox.ac.uk)

[a.] Department of Mechanical Engineering, University of Bath, Claverton Down, Bath, Somerset, BA2 7AY, United Kingdom

[b.] Department of Engineering Science, University of Oxford, Parks Road, Oxford, Oxfordshire, OX1 3PJ, United Kingdom.

* Corresponding author

Competing Interests

Declarations of interest: none

Submission declaration

This work has not been published previously and is not under consideration for publication elsewhere. Publication has been approved by both authors and it will not be published elsewhere in the same form.

Highlights

- (Eigen)strain solution for residual stress in zirconia-porcelain dental prostheses

- Thermal expansion mismatch and sintering dominate bulk stress in coping

- Phase transformation drives micro-scale residual stress at interface

- Eigenstrain gradient model closely matches phase variation found experimentally

- Stress distribution is captured well through multi-scale modelling approach

Abstract

The exceptional strength and appealing aesthetics of porcelain veneered Yttria Partially Stabilised Zirconia (YPSZ) dental prostheses, has led to the widespread adoption of these materials. However, near-interface chipping of the porcelain remains the primary failure mode. Advanced experimental techniques have recently revealed significant variations in residual stress and YPSZ phase distribution at the YPSZ-porcelain interface. Therefore, in order to improve existing understanding and effectively optimise the production of these devices, an enhanced model of the YPSZ coping that includes these newly discovered phenomena is presented in this study.

Macroscale stresses are shown to arise through the uneven temperatures within the coping during the sintering process and the coefficient of thermal expansion mismatch with the porcelain during veneering. In contrast, microscale stresses are driven by the YPSZ phase transformation and the associated volumetric expansion. The eigenstrain approach proposed here was found to demonstrate a good match between the phase variation determined experimentally, and the corresponding residual stress distribution showed an effective comparison with the empirical measurements. The proposed technique is a straightforward but powerful method for simulating this dominant mechanical behaviour, with significant potential to combine the resulting expressions into existing models. These enhanced simulations are the only viable approach for the precise, reliable and systematic optimisation of prosthesis production parameters that are needed to significantly reduce prosthesis failure rates.

Graphical abstract
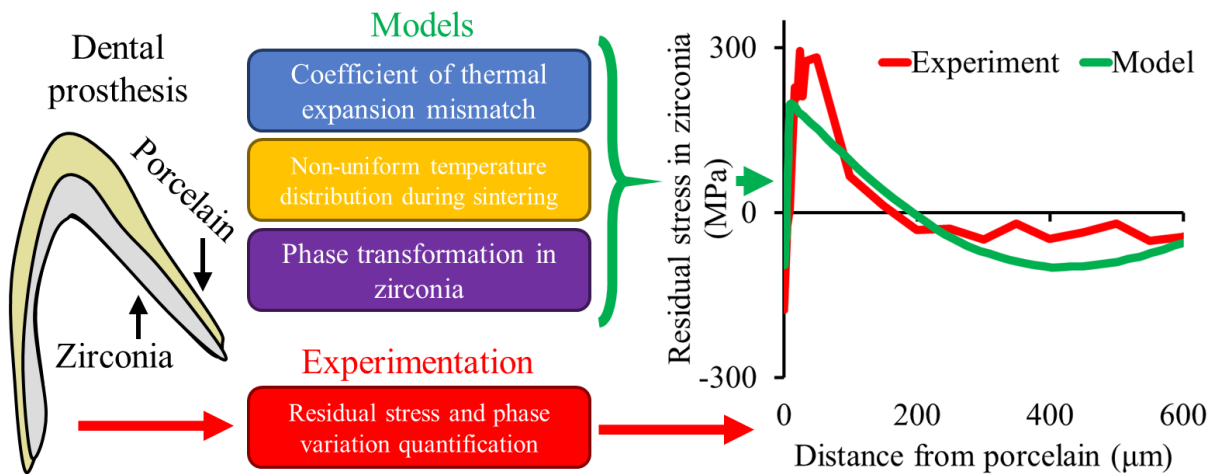
Keywords

Yttria partially stabilized zirconia, eigenstrain, dental prosthesis, residual stress, phase

transformation

CTE – Coefficient of Thermal Expansion
DIC – Digital Image Correlation
FEA – Finite Element Analysis
FIB – Focused Ion Beam
XRD – X-ray Diffraction
YPSZ – Yttria Partially Stabilised Zirconia

1. Introduction

Yttria Partially Stabilised Zirconia (YPSZ) is a high strength biocompatible ceramic that in recent years, has found increasing use in dental implant copings due to its exceptional toughness (Roehling et al., 2019). This mechanical response arises from the tetragonal (*t*) to monoclinic (*m*) phase transformation that is induced by high magnitude tensile stresses at crack tips (Garvie et al., 1975). The diffusionless atomic rearrangement is associated with a 7% volumetric expansion which absorbs energy and acts to close crack tips; resulting in a high toughness ceramic with a K_{IC} between 4 and 8 MPam$^{-0.5}$ (Turon-Vinas & Anglada, 2018).

In dental applications, the YPSZ coping is coated with a porcelain veneer to improve the aesthetic appearance and prevent wear of neighbouring teeth. However, this manufacturing approach is associated with the primary failure mode of these prostheses; near interface chipping of the porcelain veneer (Ferrari et al., 2015). The origins of this failure have been investigated in depth, and are associated with residual stress state at the interface (Masoud Allahkarami & Hanan, 2011; Baldassarri et al., 2012). This behaviour is significantly influenced by the thermal history and the Coefficient of Thermal Expansion (CTE) mismatch between the YPSZ and porcelain. The CTE of porcelain is generally chosen to be larger than that of the YPSZ, such that the near-interface porcelain is driven into a state of compression and the neighbouring YPSZ experiences a corresponding tension (Fischer et al., 2009). This approach exploits the high compressive strength of the porcelain (when compared to its tensile properties), and has been the focus of several bimetallic analytical models and Finite Element Analysis (FEA) studies (Eischen et al., 1990; Fabris et al., 2016; Guazzato et al., 2010; Timoshenko, 1925; Zhang et al., 2012).

Despite showing a good match with experimental results at larger distances from the interface, these models have been unable to fully capture the YPSZ-porcelain interface behaviour. One of the reasons for this, is that experimental characterisation had been limited to a spatial resolution of 10's – 100's of microns at best. However, recent developments in experimental methods have begun to shed light on the near-interface characteristics. This has included the use of synchrotron methods to

characterise the residual stress and phase variation in both the YPSZ and porcelain at microscale resolution, as well as Raman spectroscopy for quantification of the YPSZ phase variation at the interface (Lunt et al., 2019). The sequential and parallel ring-core Focused Ion Beam (FIB) and Digital Image Correlation (DIC) approaches have also been used to validate these experimental results at the microscale (Lunt & Korsunsky, 2015).

These studies were performed on the buccal surface (side) of the prosthesis where chipping is most commonly observed (de Lima et al., 2015; Rinke et al., 2013; Roediger et al., 2010) where the radius of curvature is at least an order of magnitude greater than the thickness of the coping. Therefore, the spherical/cylindrical form can be well approximated by that of an equibiaxially stressed plate at this position (Young et al., 2002). Approximating the system in this way has the added advantage of being described by a single positional variable which is the easiest formulation for input into existing models of the system.

These improved experimental insights have demonstrated that the high magnitude tensile stresses in the YPSZ are sufficient to induce the *t-m* phase transformation close to the interface. This relieves the residual stress in the YPSZ and drives the neighbouring porcelain into a state of mild tension. It is this effect, combined with the sequential porcelain sintering and creep induced nanovoiding, which ultimately reduces the fracture toughness of the near interface porcelain and leads to failure at this location (A. Lunt et al., 2017; A. J. G. Lunt et al., 2015).

Experimental results of this kind offer new insights for enhanced modelling of the interface, and therefore careful consideration of an effective simulation approach is required. The challenge is to identify an approach with is realistic and representative of the physical response but is sufficiently simple and adaptable as to facilitate optimisation of the production parameters.

One approach that can be used is FEA, which offers effective and efficient simulations of these types of loading conditions and deformation characteristics, provided that reliable estimates of the mechanical properties of a component or system are known. As such, quantification of the failure load presents a challenge, since the input material parameters depend greatly the on the

microstructure and residual stress state induced by processing. A method which has previously been used to overcome this obstacle has been the integration of analytical residual stress distributions into FEA using an eigenstrain (equivalent plastic strain) distribution approach (Achintha et al., 2013; A. M. Korsunsky, 2009). These models have been shown to be particularly effective at simulating residual stress distributions at surfaces and interfaces at the micro-to-nanoscale (A. M. Korsunsky et al., 2018; Enrico Salvati et al., 2016; X. Song et al., 2012) and has also been previously been successfully used to simulate phase transformations (Tirry & Schryvers, 2009).

In this paper the eigenstrain approach has been optimised and refined in order to encapsulate the phase transformation and resulting residual stress distribution within the YPSZ coping as a function of distance from the interface. This highly localised (microscale response) has then been combined with existing simulations of CTE mismatch and enhanced consideration of the non-uniform temperature variation induced in the coping during sintering. This approach captures the differing residual stress drivers across the entire YPSZ cross section (at the millimetre length scale), to offer a powerful but flexible model for the optimisation of production parameters.

2. Material and methods

In order to assess the validity of the proposed model, the residual stress and YPSZ phase distribution obtained in this study will be compared on those previously determined experimentally (A. Lunt et al., 2019). This analysis was performed on a representative incisal prosthesis which was produced from Wieland Dental Zenotec Zr bridge. A veneer of IPS e.max Ceram was applied to the YPSZ coping according to the manufacturer's instructions. Cross sections were obtained using a slow speed saw, followed by gentle polishing to minimise the influence of sample preparation on the results obtained.

Experimental analysis was then performed across the side walls of the crown in both the YPSZ and porcelain. The in-plane residual stress distribution was quantified using the ring-core FIB and DIC approach (A. J. Lunt et al., 2015). This method makes using of a FIB to mill traction free surfaces at the microscale, thereby relieving the residual stress in small cores of material in the

surface of the sample. Scanning electron microscopy images are incrementally captured during milling process to provide a record of strain change in these cores which can be quantified using DIC. The relief profiles are then compared with FEA predictions in order to estimate the residual stresses originally present.

The sequential ring-core FIB and DIC approach was performed using a 5 μm diameter core, 1 μm trench width and a 50 μm step size to determine the residual stress variation across the entire coping (E. Salvati et al., 2017). The parallel FIB and DIC approach was next applied for high resolution analysis of the residual stress distribution within the YPSZ at the interface (Baimpas et al., 2014). Eight markers of a size 3×3 μm^2 were milled using a trench width of 1 μm to give a residual stress measurement every 4 μm. Close to the interface, these results were validated using transmission synchrotron X-ray Diffraction (XRD) which was used to map lattice strain variations at a resolution of 2.8 μm (A. J. G. Lunt et al., 2016).

In order to characterise the phase variation as a function of distance from the interface, Raman spectroscopy of the sample was also performed on the coping with a measurement point every 1 μm (A. Lunt et al., 2019). This approach is based on the relative intensity of the monoclinic and tetragonal peaks which are observed in this spectrum (Clarke & Adar, 1982). The distribution was cross-validated using synchrotron XRD, by comparing the ratio of the monoclinic and tetragonal Bragg peak intensities (Toraya et al., 1984).

3. Theory and modelling

The interaction between the YPSZ and porcelain is dominated by the residual stress state within the YPSZ in a direction parallel to the interface, and therefore the following analysis has been focused on this mechanical response. In order to fully capture this behaviour, the analysis has been performed at two distinct length scales. Firstly, the global ("macro-scale") stress distribution across the entire coping is decomposed into two key effects: CTE mismatch between YPSZ and porcelain that arises as a consequence of veneering (in section 3.1), and the residual stress induced by temperature variations across the coping during YPSZ sintering (in section 3.2). The micro-scale

residual stresses induced by the phase transformation at the YPSZ-porcelain interface are next modelled using eigenstrain gradient transformation plasticity (in section 3.3). Reassembly of these three effects is then performed in order to facilitate quantitative assessment of the parameters associated with these different sources of residual stress.

It should be highlighted that the modelling outlined below is based on approximating the YPSZ-porcelain coping as an equibiaxially stressed plate, as previously exploited to great success in existing models within the literature (M. Allahkarami et al., 2010; Ni et al., 2013; Olevsky et al., 2013; Swain et al., 2019). This approximation exploits the fact that the radius of curvature of the coping is at least an order of magnitude higher than its thickness on the buccal and lingual surfaces (sides) of the prosthesis, where porcelain chipping is primarily observed (de Lima et al., 2015; Rinke et al., 2013; Roediger et al., 2010). By making use of this approach, the stress variation within the plane can be written as a function of a single positional descriptor (*x*). This variable is defined by an origin at the YPSZ-porcelain interface, with positive *x* values corresponding to the YPSZ coping and negative to the porcelain veneer.

As is the case for any approximation, experimental validation for the suitability of the approach is crucial. This validation has recently been provided in the literature, which shows nominally identical stress profiles in the two orientations being considered in this study (A. Lunt et al., 2019). Within an equibiaxial system, Mohr's circle for stress collapses to a single point, such that there are no shear stresses within this plane (Timoshenko, 1925). This is supported by the low-magnitude shear stresses determined experimentally, and as a result the shear stress within the plane will be considered to be zero in the remainder of this study.

One of the important considerations when approximating the system as equibiaxial is the use of appropriate boundary conditions. In the model below, consideration will be given to stresses and forces which are generated by coefficient of thermal mismatch, sintering and phase transformation. This forms a strong basis for further analysis of the interaction of external forces, but these effects will not be analysed in this instance. Therefore, given that no external forces are being applied, the

sum of stresses over the cross section must be balanced when the coping is in stable condition. This approach has been used and described widely within the literature (Aydiner et al., 2001; Gardon, 1980; Indenbom, 1954; A. Korsunsky et al., 2016) and is based around the idea that if there were unbalanced forces, the resultant moment would cause the plate to bend to a point where equilibrium is achieved.

3.1. Coefficient of thermal expansion mismatch

Analytical modelling of the residual stress distribution at the YPSZ-porcelain interface has previously been performed by approximating the system by a bi-material strip (Asaoka & Tesk, 1990; Dehoff & Anusavice, 1989; Swain, 2009). This analysis can capture the linear variation of strain induced in both YPSZ and porcelain by the CTE mismatch which results in tensile near-interface stress in YPSZ, and compressive in porcelain.

In the analysis that follows the simple bending approach (Timoshenko, 1925) has been used to determine the residual stress distribution in both materials in the direction parallel to the interface as a function of the normal distance from the interface. Complete expressions for the stress profiles have previously been presented in the literature (Eischen et al., 1990) and demonstrate that these are dependent upon the thickness of YPSZ ($L^Z = 625$ μm) and porcelain ($L^P = 925$ μm), the CTE's of the two materials (A. Lunt et al., 2019) and the post sintering temperature change (750°C → 25°C). Representative estimates of the elastic modulus of YPSZ $\left(E_Z^{Eff}\right)$ and porcelain $\left(E_P^{Eff}\right)$ are also required, which can be represented well by the plane strain expressions:

$$E_Z^{Eff} = \frac{E_Z}{(1 + \nu_Z)(1 - 2\nu_Z)} = 404 \text{ GPa,} \tag{1}$$

$$E_P^{Eff} = \frac{E_P}{(1 + \nu_P)(1 - 2\nu_P)} = 96 \text{ GPa.} \tag{2}$$

The linearly varying residual stress distributions resulting from this analysis are shown in Figure 1 in which the near interface YPSZ is seen to be in tension (of ≈ 110 MPa) and the near interface porcelain is found to be in a state of mild compression (of ≈ −30 MPa). These distributions do not match the distributions observed experimentally (A. Lunt et al., 2019) and

suggest that other factors are influencing the residual stress state at the interface. In the case of YPSZ, the sintering approach is known to induce macro-scale variations in residual stress that are present in addition to the CTE mismatch. In porcelain, this is associated with the layering routine applied to the YPSZ coping which will not be considered in more detail here.
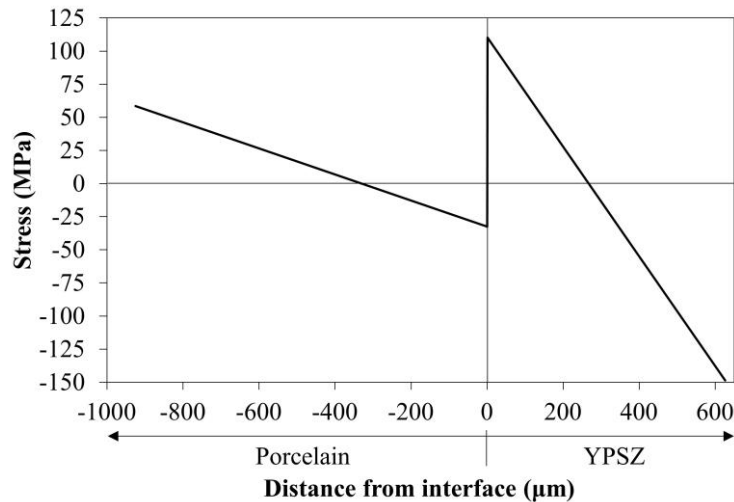

Figure 1. Stress variation across the YPSZ-porcelain interface predicted by CTE mismatch.

3.2. YPSZ sintering stresses

During the manufacture of the coping, the YPSZ lightly pre-sintered green body is placed into a furnace and heated to $1600°C$ to sinter the component. This process is associated with a $\approx 20\%$ shrinkage (densification) of the YPSZ at a critical densification temperature T_D which is dependent upon the YPSZ grain size and elemental composition (Hsueh et al., 1986; Stawarczyk et al., 2013). This structural change is associated with a large increase in strength and fracture toughness (Sato et al., 1996).

Although sintering is typically performed using a slow heating rate, the extremely low thermal diffusivity of 5 mol% YPSZ ($D = 2.2 \times 10^{-7} \mathrm{m}^2\mathrm{s}^{-1}$ (Basu, 2005)) results in temperature gradients between the surface of the coping and the core. Consequently, the complete sintering and the associated shrinkage do not occur uniformly across the coping. This results in strain mismatch and induces a residual stress distribution that varies with time and temperature in accordance with the solution of the transient thermal conduction equation. Previous studies have demonstrated that the residual stress distribution that arises in this kind of sintering operations is near parabolic in profile

(Grabner, 1978), with compressive stresses present within the core, and tensile stresses in the near-surface region. The magnitude of this residual stress distribution in YPSZ is particularly sensitive to the cooling rate applied, and sintering fracture can be induced if high heating or cooling rates are applied (Magnani & Brillante, 2005).

In order to understand the distribution of residual stress within the coping, consideration must first be given to the temperature distribution within the coping cross section, $T(x, t)$, as a function of position (x) and time (t). The 1D heat conduction equation can be used to determine this distribution in the following form:

$$\frac{\partial T(x, t)}{\partial T} = D \frac{\partial^2 T(x, t)}{\partial x^2}. \tag{3}$$

Separation of variables and Fourier series representation can be used to solve this equation using the appropriate boundary conditions. This approach has been covered in detail in the literature (Kreyszig, 2019).

At this stage of the assessment it is important to discuss the limits in which the form of the 1D heat equation shown in Equation 3 remains valid. Intrinsically, within this formulation there is an approximation that the thermal diffusivity D is constant within the temperature range under consideration (in other words, it does not depend upon temperature or time). Fortunately, the high temperature thermal characteristics of YPSZ are generally well-known, as this material has found extensive use as a thermal barrier coating (Chen, 2006). These studies have demonstrated that in general the thermal diffusivity of YPSZ shows little variation with temperature (Brandon & Taylor, 1989; Xiwen Song et al., 2011). In fact, a YPSZ alloy with similar Y_2O_3 weight percent was found to show only a ±6.4% variation in D between 200°C and 1200°C. The approximation of constant D for the subsequent analysis is therefore likely to be realistic in allowing the approximate form of the temperature profile within the coping to be determined.

One further phenomenon that needs to be considered when making use of the approximation of the 1D heat equation, is the phase stability of the material being analysed. During phase transitions, latent heat effects will absorb or release energy and have a significant impact on the temperature

variation within the sample. Dental YPSZ is specifically alloyed such that the room temperature phase is metastable tetragonal *t'* which is retained up to temperatures of 1400°C (Krause et al., 2016). The unstable nature of this phase means that the material is able to transform to a monoclinic *m* phase with the application of tensile stresses. This transformation absorbs energy and is associated with a 7% volume expansion which acts to close crack tips and gives the material an exceptional toughness for a ceramic (Garvie et al., 1975). This property is one of the main reasons that YPSZ has found widespread use in biomedical systems such as hip joints and dental implants.

For temperatures above 1400°C the metastable *t'* phase of YPSZ transforms to *m* and the yttrium rich *t''*. Studies have shown that at 1600°C, this phase change is approximately 1% after 10 hours (Lipkin et al., 2013). Given that the YPSZ in this study is raised above 1400°C for a total duration of approximately 30 minutes, the % phase change within the coping is expected to be much smaller than 1%. Such a conclusion is perhaps unsurprising, as the sintering cycle has been selected to maximise densification during the sintering process as well as the toughness of the YPSZ coping (by minimising the phase transformation). The approximation of constant phase is therefore likely to be valid, meaning that the results obtained from the 1D heat equation are representative of the temperature profiles present within the coping.

In order to gain insight into the likely temperature distribution induced within the coping cross section during sintering, one of the simplest solutions that can be exploited is based on an instantaneous temperature rise. This analysis is based on holding the prosthesis at 25°C and imposing boundary conditions at 1600°C at either surface (i.e. $\Delta T = 1575°C$) and has a solution:

$$T(x,t) = 1600 - \sum_{m=1}^{\infty} \frac{4\Delta T}{(2m-1)\pi} e^{-t\left(\frac{(2m-1)c\pi}{L^Z}\right)^2} \sin\left[(2m-1)\frac{\pi x}{L^Z}\right], \qquad (4)$$

where $c = \sqrt{D}$. The temperature variation at different time intervals is shown in Figure 2. This plot demonstrates that after a short time period (≈ 5 s), the temperature distribution is well approximated by a sine curve with a magnitude equal to the difference between the external

temperature and the central temperature. In the case of a reduced heating rate, a similar sinusoidal distribution is expected but with a magnitude dependent upon the heating rate applied.
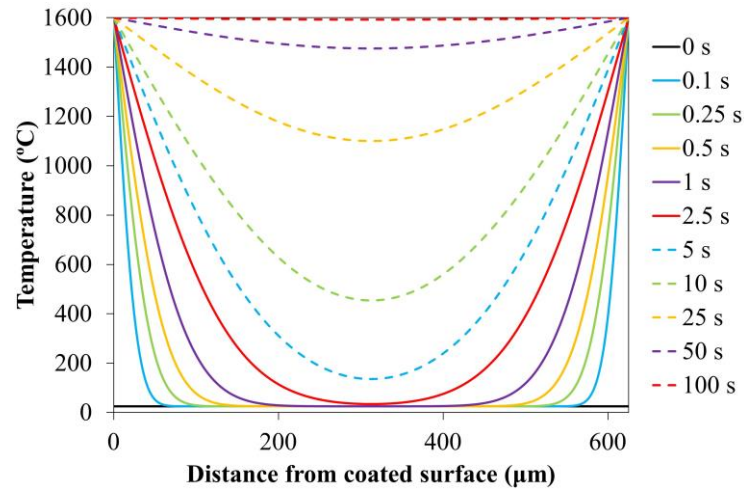

Figure 2. Temperature distributions within the YPSZ coping as a function of time after an instantaneous temperature increase at the boundaries to 1600℃.

One additional factor that needs to be assessed for the suitability of the proposed sinusoidal temperature distribution, is the sensitivity of the 1D heat equation to the thermal diffusivity parameter D. Although significant analysis has been performed on YPSZ alloys designed for thermal barrier coatings, very few peer reviewed articles have provided estimates of D for dental YPSZ. A review of the literature revealed that the value of $D = 2.2 \times 10^{-7}$ m^{2}s^{-1} for 5 mol% Y$_2$O$_3$ (Basu, 2005) was likely to be most representative of the material used in this study. The smallest published estimate for D for dental YPSZ was 1×10^{-7} m^{2}s^{-1} (O'Brien, 2002) and the largest was 7.5×10^{-7} m^{2}s^{-1} (Swain, 2009). Therefore, the analysis outlined above was repeated using these two extreme cases. These calculations revealed that the temperature profiles obtained are nominally identical, with offsets in the associated dwell times. In the case of $D = 1 \times 10^{-7}$ m^{2}s^{-1} a sinusoidal temperature distribution was obtained after ≈10 s and for $D = 7.5 \times 10^{-7}$ m^{2}s^{-1} it was ≈1 s. Given that the nominal sintering time of the coping is on the order of hours, the approximation of a sinusoidal temperature variation therefore remains valid within the range of known literature estimates of D.

Having established the nominal temperature distribution profile within the coping during sintering, the relationship between residual stress (or, rather, the underlying misfit strain, or eigenstrain) and this distribution needs to be established. In materials with a distinct mechanical property transition temperature, one of the simplest and most effective approaches which can be exploited to determine this relationship is based on the *instant freeze model* pioneered by Indenbom (Indenbom, 1954). This approach is based on separating the total strain $\varepsilon^T(x)$ into three additive components, elastic strain $\varepsilon^E(x)$, viscous strain $\varepsilon^V(x)$ and thermal strain $\varepsilon^H(x)$:

$$\varepsilon^T(x) = \varepsilon^E(x) + \varepsilon^V(x) + \varepsilon^H(x). \tag{5}$$

Viscous strain is a parameter that was originally coined by Indenbom to refer to the strains that are permanent 'frozen in' the green body below a critical densification temperature T_D. This descriptor is more generally referred to as eigenstrain, with the equivalence between these two terms being highlighted in a number of literature sources (Aydiner et al., 2001; A. Korsunsky et al., 2016).

Therefore, from this point onwards the effective viscous strain will subsequently be referred to as eigenstrain $\varepsilon^*(x)$; a formulation that was pioneered by Mura (Mura, 1987) to describe permanent/transformation strains as a source of residual stress. This approach has been shown to be useful in simulating the response of a material to a broad range of physical changes or interactions, including laser shock peening (Achintha et al., 2013), at interfaces (Zhong & Meguid, 1996) or around inclusions (Takao et al., 1981).

Eigenstrain modelling is reliant upon providing a physical interpretation for the permanent strain distribution within a body of interest. In the case of a cooling body, Indenbom's model is particularly effective. This formulation is based on the presumption that on one side of the transition temperature (below in the case of sintering) the material does not sustain any elastic strain (and therefore that stress is zero). Densification then proceeds from either surface until this front reaches the centre of the body and the entire component is at a temperature above T_D. From this point, the eigenstrain distribution is fixed and the final residual stress state at room temperature arises from the interplay between this distribution and the changing thermal and elastic strains.

One study which has recently used this approach to great effect has been an analysis of thermal tempering of bulk metallic glass plates by Aydiner et al. (Aydiner et al., 2001) in which similar trigonometric thermal distributions are observed. The principal difference between the results of this approach and those presented here, is that an increase in strength and stiffness is observed during cooling below the glass transition temperature in this study, rather than the increase in strength observed when heating above the critical densification temperature. With this distinction accounted for, the analysis presented in this study can be used by simply changing the sign of the eigenstrain distribution. The resulting stress distribution has the form:

$$\sigma(x) = \alpha_Z E_Z^{Eff} T(x, t_D) + \sigma_{Bal}, \tag{6}$$

where t_D is the time at which full densification occurs, i.e. when the minimum temperature in the cross section is equal to T_D. The term σ_{Bal} is identical to that proposed by Aydiner (Aydiner et al., 2001) and is required to ensure that stress distribution is in equilibrium across the plate cross section i.e. $\int_0^L \sigma(x)dx = 0$. Since both T_D and the external temperature at a time t_D are unknown, a trigonometric approximation of the form:

$$\sigma(x) = -\alpha_Z E_Z^{Eff} \Lambda \sin\frac{\pi x}{L^Z} + \sigma_{Bal}, \tag{7}$$

can instead be used, where Λ is the difference between the external temperature and T_D at a time t_D. In order to determine a numerical estimate of this parameter, comparison between the experimental and analytical residual stress profiles can be used. This process requires the addition of the linear residual stress distribution resulting from CTE mismatch to provide estimates of the total macroscopic stress distribution as shown in Figure 3.
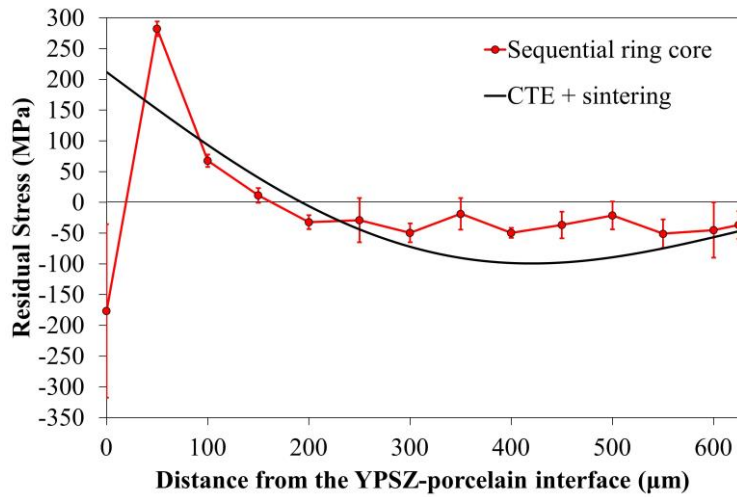
Figure 3. Residual stress as a function of distance from the YPSZ-porcelain interface. Shown are the experimental results obtained through sequential ring-core milling (markers) (A. Lunt et al., 2019) and the predicted distribution analytically based on the combination of CTE mismatch and sintering.

The fitted value of Λ was found to be 38 K, and the resulting stress profile was found to show a satisfactory match with the experimental results for most of the coping cross section. The largest deviation between these two profiles is observed at the YPSZ-porcelain interface, at the location where the tetragonal to monoclinic phase transformation is induced. This suggests that the volume expansion associated with the phase transformation has influenced the residual stress state at this location, and further modelling of this behaviour is presented in section 3.3. Some discrepancy is also observed at the points 50 μm and $350 - 500$ μm from the interface, indicating that the profile sharpness has not been fully captured by the two residual stress sources considered in this analysis.

3.3. Transformation boundary layer modelling

Limited experimental observations into the location and extent of the tetragonal to monoclinic phase transformation has previously prevented this effect from being included in the analysis of residual stress at the YPSZ-porcelain interface. The principal difficulty has been the fact that the related phenomena play out at extremely short length scales and recent experimental developments have been necessary to elucidate this behaviour. The present section is devoted to the derivation of the boundary layer model for the transformation-induced inelastic strain (eigenstrain) that allows comparison with the monoclinic volume fraction (V_m) distributions obtained experimentally. These results can then be combined with those presented in section 3.1 and 3.2 to provide complete insight into the residual stress state in YPSZ.

As shown in Figure 3, the CTE mismatch and sintering residual stress generation approach fails to predict the very steep stress gradients observed at the YPSZ-porcelain interface. In fact, these high magnitude localised stresses are similar to those observed at crack tips (McMeeking & Evans, 1982), and those have previously been shown to be sufficient to induce the tetragonal to monoclinic phase transformation. The atomic rearrangement associated with the phase change is diffusionless and is therefore equivalent to inelastic stress-free straining, which can be simulated effectively through the use of eigenstrain (A. M. Korsunsky, 2009). The magnitude of the eigenstrain distribution can be considered to be equivalent to the extent of transformation at a given position and can therefore be used to link the phase transformation to the mechanical state.

In this section the boundary layer solution for the 1D distribution of stress and strain component parallel to the YPSZ-porcelain interface is described as a function of normal distance from the interface (x) within the narrow band of material where the steep stress gradient is present. An estimate of the total strain (here meaning the sum of elastic strain and eigenstrain) within YPSZ at the interface (ε_0^T) based on the CTE mismatch cooling from 750 °C → 25°C is given as:

$$\varepsilon_0^T = \varepsilon^T(0) = (\alpha_{Zir} - \alpha_{Por})(750 - 25) = 1.09 \times 10^{-3}. \qquad (8)$$

Critical examination of Figure 3 indicates that the analytical macroscale residual stress estimate at the interface is ≈ 210 MPa. However, due to the activation of phase transformation the actual residual stress measured at this location is compressive and, due to scatter, has a magnitude in the range $25 - 175$ MPa (A. Lunt et al., 2019). The average value of this stress is ≈ -100 MPa. Therefore, the stress change induced by the tetragonal to monoclinic phase transformation at the interface can be approximated as 310 MPa. By way of estimate, this corresponds to an eigenstrain value of $\varepsilon^*(0) \approx 7.7 \times 10^{-4}$.

Using the approximations outlined above, the form of the expected eigenstrain $\varepsilon^*(x)$ profile can be determined from energy considerations and variational calculus. In the subsequent analysis, the total strain will be assumed to be equal to the sum of elastic strain and eigenstrain. The elastic strain energy is therefore given as:

$$U^E = \frac{1}{2} E_{eff} \int_0^L [\varepsilon^E(x)]^2 dx = \frac{1}{2} E_{eff} \int_0^L [\varepsilon^T(x) - \varepsilon^*(x)]^2 dx, \qquad (9)$$

where L is the width of the region of interest (boundary layer). In addition to this elastic expression, two further energy terms need to be considered. The first is associated with the energy reduction induced by strain gradient plasticity (Mura & Koya, 1992) given by:

$$U^{SG} = \frac{1}{2} E_{eff} \int_0^L \left[\frac{d\varepsilon^*}{dx}\right]^2 \ell^2 dx = \frac{1}{2} E_{eff} \int_0^L \varepsilon_{,x}^{*\,2} \ell^2 dx, \qquad (10)$$

where ℓ is the strain gradient material length scale (Hutchinson & Fleck, 1997) and $\varepsilon_{,x}^*(x)$ is the rate of change of eigenstrain with respect to x. The origin of this energy penalty lies in the fact that the deformation of solid regions that are closely neighbouring at the micron-scale cannot be entirely independent: sharp transitions become 'blurred' into local gradients. The total energy of the system is therefore not simply the sum of contributions from sub-volumes, but also depends upon the steepness of transition (strain gradient) between them. In the present treatment, eigenstrain gradient plays a role similar to the plastic strain gradient in the Hutchinson and Fleck strain gradient plasticity theory (Hutchinson & Fleck, 1997).

The second energy reduction term is the Gibbs free energy reduction due to the phase transformation:

$$U^{Tr} = \frac{1}{2} E_{eff} \int_0^L [\varepsilon^*(x)]^2 \Gamma dx, \tag{11}$$

where Γ is the coefficient which relates the square of the eigenstrain to the amount of energy required to induce the phase transformation per unit volume.

These expressions can be combined to give an expression for the total energy:

$$U^T = U^E - U^{SG} - U^{Tr} = \frac{E_{eff}}{2} \int_0^L \left[(\varepsilon^T(x) - \varepsilon^*(x))^2 - \ell^2 (\varepsilon^*_{,x}(x))^2 - (\varepsilon^*(x))^2 \Gamma \right] dx. \tag{12}$$

Rearrangement gives:

$$U^T = E_{eff} \int_0^L \left[\frac{1}{2} (\varepsilon^T(x))^2 - \varepsilon^*(x)\varepsilon^T(x) + \frac{1}{2}(1 - \Gamma)(\varepsilon^*(x))^2 - \frac{1}{2}\ell^2 (\varepsilon^*_{,x}(x))^2 \right] dx. \tag{13}$$

In order to minimise the total energy, the derivative of U^T must be set equal to zero, such that:

$$\delta U^T = \frac{dU^T}{d\varepsilon^*} \delta \varepsilon^* = 0. \tag{14}$$

Therefore:

$$\delta U^T = 0 = E_{eff} \int_0^L [-\varepsilon^T(x) + (1 - \Gamma)\varepsilon^*(x)]\delta \varepsilon^* dx$$

$$- E_{eff} \int_0^L \ell^2 \varepsilon^*_{,x}(x)\delta \varepsilon^*_{,x} dx. \tag{15}$$

In order to remove $\delta \varepsilon^*_{,x}$ from this expression, integration by parts can be applied to the 2$^{\text{nd}}$ integral:

$$\int_0^L \ell^2 \varepsilon^*_{,x}(x)\delta \varepsilon^*_{,x} dx = \left[\varepsilon^*_{,x}(x)\delta \varepsilon^*_{,x} \right]_0^L - \int_0^L \ell^2 \varepsilon^*_{,xx}(x)\delta \varepsilon^* dx, \tag{16}$$

where $\varepsilon^*_{,xx}(x)$ is the second derivative of eigenstrain with respect to x. In order to ensure that U^T is a minimum for any value of $\delta \varepsilon^*$, the term associated with limit substitution must equal zero. This results in the so-called 'natural' boundary conditions of $\varepsilon^*_{,x}(L) = \varepsilon^*_{,x}(0) = 0$. Back substitution then gives:

$$0 = E_{eff} \int_0^L [-\varepsilon^T(x) + (1 - \Gamma)\varepsilon^*(x) + \ell^2 \varepsilon^*_{,xx}(x)]d\varepsilon^* dx. \tag{17}$$

Since $\delta\varepsilon^*$ can take any value, this expression is only guaranteed to be true when the expression in the square brackets is equal to zero. This results in the Euler differential equation for this system:

$$\varepsilon^*_{,xx}(x) + \frac{(1-\Gamma)}{\ell^2}\varepsilon^*(x) = \frac{1}{\ell^2}\varepsilon^T(x). \tag{18}$$

This equation has the complementary function solution:

$$\varepsilon^*_{CF}(x) = Ae^{-\omega x} + Be^{\omega x}, \tag{19}$$

where A and B are constants to be found, and $\omega^2 = (\Gamma - 1)/\ell^2$.

In order to determine the particular integral for the Euler equation, the form of the total strain distribution needs to be considered. Within the thin (≈ 10 µm) boundary layer the total strain variation can be approximated as linear, with the interface strain equal to that derived in Equation 8. Therefore, it is possible to write:

$$\varepsilon^*_{PI}(x) = \frac{\varepsilon^T_0 + Cx}{1 - \Gamma}, \tag{20}$$

where C is another unknown constant to be found. In order to determine the expressions for A, B and C, the 'natural' boundary conditions can be used, along with the fact that the phase transformation at L is expected to be zero, i.e. $\varepsilon^*(L) = 0$. The resulting eigenstrain distribution is given by:

$$\varepsilon^*(x) = \frac{\varepsilon^T_0}{1-\Gamma}\left[1 + \frac{(1-e^{\omega L})e^{-\omega x} + (1-e^{-\omega L})e^{\omega x} + \omega x(e^{-\omega L} - e^{\omega L})}{2 - e^{-\omega L} - e^{\omega L} - \omega L(e^{-\omega L} - e^{\omega L})}\right]. \tag{21}$$

This expression can then be simplified using the hyperbolic functions $\sinh(x)$ and $\cosh(x)$:

$$\varepsilon^*(x) = \frac{\varepsilon^T_0}{1-\Gamma}\left[1 - \frac{\sinh\omega\left(\frac{L}{2} - x\right) + \omega x \cosh\frac{\omega L}{2}}{\omega L \cosh\frac{\omega L}{2} - \sinh\frac{\omega L}{2}}\right]. \tag{22}$$

In order to obtain estimates of L, Γ and ℓ, this expression can then be compared to the monoclinic phase variation determined experimentally (A. Lunt et al., 2019). This fitting process also requires the estimate of the interface eigenstrain to be incorporated, $\varepsilon^*(0) \approx 7.7 \times 10^{-4}$. The results of this analysis are shown in comparison to the monoclinic volume fraction distribution in Figure 4. The

optimum values of the system parameters were found to be $L = 10.7 \pm 0.3$ µm, $\Gamma = 1.55 \pm 0.06$ and $\ell = 2.88 \pm 0.15$ µm.
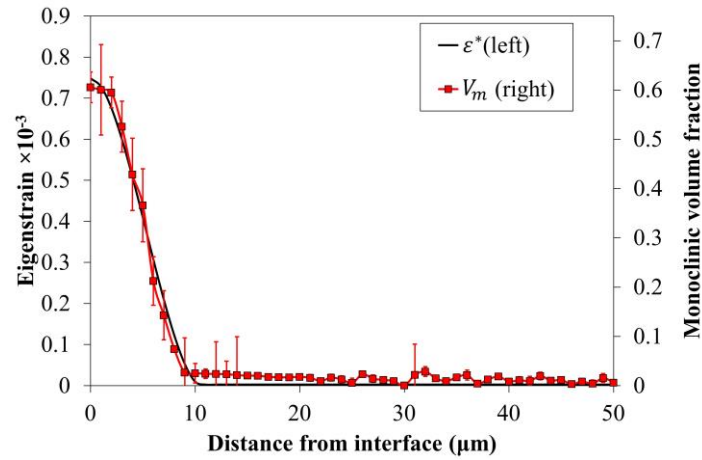

Figure 4. Comparison between the analytical eigenstrain distribution (left) and monoclinic volume fraction determined using Raman spectroscopy (right) (A. Lunt et al., 2019).

The very close similarity observed between the shape of the analytically derived eigenstrain distribution and Raman spectroscopy experimental results suggests that the present energy minimisation captures well the physical processes that take place in the near-interface region. The eigenstrain variation found can be combined with the macro-scale formulation for the stress state within the prosthesis to generate an improved understanding of the overall mechanical state in the coping as shown in Figure 5.
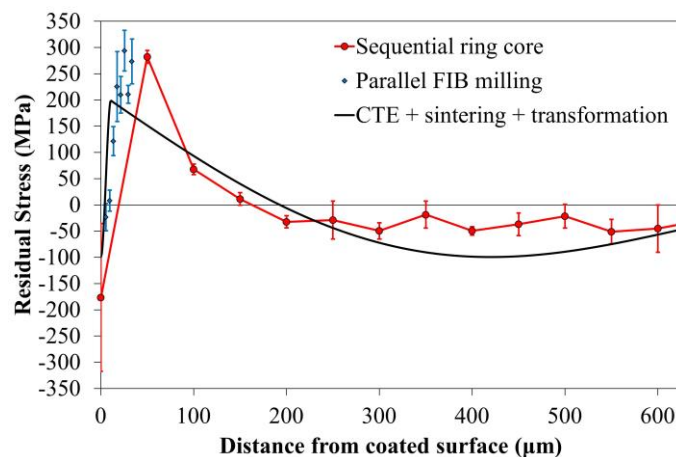

Figure 5. Residual stress as a function of distance from the YPSZ-porcelain interface. The experimental results obtained through sequential ring-core and parallel FIB milling are shown (A. Lunt et al., 2019) along with the complete analytical solution.

4. Discussion and conclusions

In this article, analytical modelling of the residual stress distribution in a YPSZ dental prosthesis have been presented. This distribution has been decomposed into the macroscale effects of coefficient of thermal expansion mismatch and residual stresses induced during sintering. as well as phase transformation characteristics induced within a few microns of the interface. Figure 5 demonstrates that there is a satisfactory match between the experimental results and the model over much of the cross section. The main deviation between these two profiles is observed at $\approx 20 - 70$ μm from the interface, where the model underpredicts the magnitude of residual stress identified experimentally. The origins of this deviation are unclear but may be associated with the influence of thermal tempering, or the multi-layering porcelain manufacture approach which have not been considered here. Despite these differences, the general trends in residual stress have been captured effectively by combining the three sources outlined in section 3.

The eigenstrain approach that has been implemented has been shown to be particularly successful at emulating the influence of the this diffusionless transformation. This technique provides a flexible analytical method which can be combined with existing FEA models of YPSZ-porcelain dental prostheses in order to facilitate optimisation of a range of production parameters. At larger (millimetre) length scales this could include the consideration of different thermal expansion coefficients or thermal histories. Locally, the impact of differing YPSZ characteristics such as diffusivity and Gibbs free energy of the *t-m* transformation can also be analysed and assessed. However, it should be noted that in order to fully encapsulate the system response to these varying conditions, enhanced simulations of the veneering process, including the degradation of mechanical properties at high temperatures and stresses is required. Development of the tools necessary to encapsulate this response are ongoing, and will be combined with the YPSZ simulations in subsequent publications.

One aspect of this approach that is worth remarking on is the successful use of eigenstrain as a parameter that describes the diffusionless phase transformation in YPSZ, which has been combined

with the strain gradient plasticity formulation for the first time. This opens interesting possibilities for modelling many other processes and phenomena related to martensitic transformation, including quenching of carbon steels, shape memory alloys and polymers, and many other effects.

References

Achintha, M., Nowell, D., Shapiro, K., & Withers, P. J. (2013). Eigenstrain modelling of residual stress generated by arrays of laser shock peening shots and determination of the complete stress field using limited strain measurements. *Surface and Coatings Technology*, *216*, 68–77. https://doi.org/10.1016/j.surfcoat.2012.11.027

Allahkarami, M., Bale, H. A., & Hanan, J. C. (2010). Analytical Model for Prediction of Residual Stress in Zirconia-Porcelain Bi-Layer. In *Advances in Bioceramics and Porous Ceramics III* (pp. 19–26). John Wiley & Sons, Ltd. https://doi.org/10.1002/9780470944028.ch2

Allahkarami, Masoud, & Hanan, J. C. (2011). Mapping the tetragonal to monoclinic phase transformation in zirconia core dental crowns. *Dental Materials*, *27*(12), 1279–1284. https://doi.org/10.1016/j.dental.2011.09.004

Asaoka, K., & Tesk, J. A. (1990). Transient and Residual Stress in a Porcelain-Metal Strip. *Journal of Dental Research*, *69*(2), 463–469. https://doi.org/10.1177/00220345900690020901

Aydiner, C. C., Üstündag, E., & Hanan, J. C. (2001). Thermal-tempering analysis of bulk metallic glass plates using an instant-freezing model. *Metallurgical and Materials Transactions A*, *32*, 2709–2715. https://doi.org/10.1007/s11661-001-1023-8

Baimpas, N., Lunt, A. J. G., Dolbnya, I. P., Dluhos, J., & Korsunsky, A. M. (2014). Nano-scale mapping of lattice strain and orientation inside carbon core SiC fibres by synchrotron X-ray diffraction. *Carbon*, *79*, 85–92. https://doi.org/10.1016/j.carbon.2014.07.045

Baldassarri, M., Stappert, C. F. J., Wolff, M. S., Thompson, V. P., & Zhang, Y. (2012). Residual stresses in porcelain-veneered zirconia prostheses. *Dental Materials*, *28*(8), 873–879. https://doi.org/10.1016/j.dental.2012.04.019

Basu, B. (2005). Toughening of yttria-stabilised tetragonal zirconia ceramics. *International Materials Reviews*, *50*(4), 239–256. https://doi.org/10.1179/174328005X41113

Brandon, J. R., & Taylor, R. (1989). Thermal properties of ceria and yttria partially stabilized zirconia thermal barrier coatings. *Surface and Coatings Technology*, *39–40*, 143–151. https://doi.org/10.1016/0257-8972(89)90049-2

Chen, L. B. (2006). Yttria-stabilized zirconia thermal barrier coatings—A review. *Surface Review and Letters*, *13*(05), 535–544. https://doi.org/10.1142/S0218625X06008670

Clarke, D. R., & Adar, F. (1982). Measurement of the crystallographically transformed zone produced by fracture in ceramics containing tetragonal zirconia. *Journal of the American Ceramic Society*, *65*(6), 284–288.

de Lima, E., Meira, J. B. C., Özcan, M., & Cesar, P. F. (2015). Chipping of Veneering Ceramics in Zirconium Dioxide Fixed Dental Prosthesis. *Current Oral Health Reports*, *2*(4), 169–173. https://doi.org/10.1007/s40496-015-0066-7

Dehoff, P. H., & Anusavice, K. J. (1989). Tempering Stresses in Feldspathic Porcelain. *Journal of Dental Research*, *68*(2), 134–138. https://doi.org/10.1177/00220345890680020701

Eischen, J. W., Chung, C., & Kim, J. H. (1990). Realistic Modeling of Edge Effect Stresses in Bimaterial Elements. *Journal of Electronic Packaging*, *112*(1), 16–23. https://doi.org/10.1115/1.2904333

Fabris, D., Souza, J. C. M., Silva, F. S., Fredel, M., Mesquita-Guimarães, J., Zhang, Y., & Henriques, B. (2016). The bending stress distribution in bilayered and graded zirconia-based dental ceramics. *Ceramics International*, *42*(9), 11025–11031. https://doi.org/10.1016/j.ceramint.2016.03.245

Ferrari, M., Sorrentino, R., Cagidiaco, C., Goracci, C., Vichi, A., Gherlone, E., & Zarone, F. (2015). Short-term clinical performance of zirconia single crowns with different framework designs: 3-year clinical trial. *Am. J. Dent*, *28*(4), 235–240.

Fischer, J., Stawarzcyk, B., Trottmann, A., & Hämmerle, C. H. F. (2009). Impact of thermal misfit on shear strength of veneering ceramic/zirconia composites. *Dental Materials*, *25*(4), 419–423. https://doi.org/10.1016/j.dental.2008.09.003

Gardon, R. (1980). CHAPTER 5—Thermal Tempering of Glass. In D. R. Uhlmann & N. J. Kreidl (Eds.), *Glass Science and Technology* (Vol. 5, pp. 145–216). Elsevier. https://doi.org/10.1016/B978-0-12-706705-6.50010-2

Garvie, R. C., Hannink, R. H., & Pascoe, R. T. (1975). Ceramic steel? *Nature*, *258*(5537), 703. https://doi.org/10.1038/258703a0

Grabner, L. (1978). Spectroscopic technique for the measurement of residual stress in sintered Al2O3. *Journal of Applied Physics*, *49*(2), 580–583. https://doi.org/10.1063/1.324682

Guazzato, M., Walton, T. R., Franklin, W., Davis, G., Bohl, C., & Klineberg, I. (2010). Influence of thickness and cooling rate on development of spontaneous cracks in porcelain/zirconia structures. *Australian Dental Journal*, *55*(3), 306–310. https://doi.org/10.1111/j.1834-7819.2010.01239.x

Hsueh, C.-H., Evans, A. G., & Mcmeeking, R. M. (1986). Influence of Multiple Heterogeneities on Sintering Rates. *Journal of the American Ceramic Society*, *69*(4), C-64-C–66. https://doi.org/10.1111/j.1151-2916.1986.tb04752.x

Hutchinson, J. W., & Fleck, N. A. (1997). Strain gradient plasticity. In *Advances in applied mechanics* (Vol. 33, pp. 295–361). Academic.

Indenbom, V. L. (1954). Theory of Tempering of Glass. *Zh. Tekh. Fiz*, *24*, 925–928.

Korsunsky, A. M. (2009). Eigenstrain analysis of residual strains and stresses. *The Journal of Strain Analysis for Engineering Design*, *44*(1), 29–43. https://doi.org/10.1243/03093247JSA423

Korsunsky, A. M., Salvati, E., Lunt, A. G. J., Sui, T., Mughal, M. Z., Daniel, R., Keckes, J., Bemporad, E., & Sebastiani, M. (2018). Nanoscale residual stress depth profiling by Focused Ion Beam milling and eigenstrain analysis. *Materials & Design*, *145*, 55–64. https://doi.org/10.1016/j.matdes.2018.02.044

Korsunsky, A., Sui, T., Salvati, E., George, E. P., & Sebastiani, M. (2016). Experimental and modelling characterisation of residual stresses in cylindrical samples of rapidly cooled bulk

metallic glass. *Materials & Design*, *104*, 235–241.

https://doi.org/10.1016/j.matdes.2016.05.017

Krause, A. R., Garces, H. F., Dwivedi, G., Ortiz, A. L., Sampath, S., & Padture, N. P. (2016).

Calcia-magnesia-alumino-silicate (CMAS)-induced degradation and failure of air plasma

sprayed yttria-stabilized zirconia thermal barrier coatings. *Acta Materialia*, *105*, 355–366.

https://doi.org/10.1016/j.actamat.2015.12.044

Kreyszig, E. (2019). *Advanced Engineering Mathematics*. John Wiley & Sons, Limited.

Lipkin, D. M., Krogstad, J. A., Gao, Y., Johnson, C. A., Nelson, W. A., & Levi, C. G. (2013). Phase

Evolution upon Aging of Air-Plasma Sprayed t′-Zirconia Coatings: I—Synchrotron X-Ray

Diffraction. *Journal of the American Ceramic Society*, *96*(1), 290–298.

https://doi.org/10.1111/j.1551-2916.2012.05451.x

Lunt, A. J., Baimpas, N., Salvati, E., Dolbnya, I. P., Sui, T., Ying, S., Zhang, H., Kleppe, A. K.,

Dluhoš, J., & Korsunsky, A. M. (2015). A state-of-the-art review of micron-scale spatially

resolved residual stress analysis by FIB-DIC ring-core milling and other techniques. *The

Journal of Strain Analysis for Engineering Design*, *50*(7), 426–444.

https://doi.org/10.1177/0309324715596700

Lunt, A. J. G., & Korsunsky, A. M. (2015). A review of micro-scale focused ion beam milling and

digital image correlation analysis for residual stress evaluation and error estimation. *Surface

and Coatings Technology*, *283*, 373–388. https://doi.org/10.1016/j.surfcoat.2015.10.049

Lunt, A. J. G., Mohanty, G., Neo, T. K., Michler, J., & Korsunsky, A. M. (2015). Microscale

resolution fracture toughness profiling at the zirconia-porcelain interface in dental

prostheses. *Micro+Nano Materials, Devices, and Systems*, *9668*, 96685S.

https://doi.org/10.1117/12.2199217

Lunt, A. J. G., Salvati, E., Ma, L., Dolbyna, I. P., Neo, T. K., & Korsunsky, A. M. (2016). Full in-

plane strain tensor analysis using the microscale ring-core FIB milling and DIC approach.

Journal of the Mechanics and Physics of Solids, *C*(94), 47–67.

https://doi.org/10.1016/j.jmps.2016.03.013

Lunt, A., Salvati, E., Baimpas, N., Dolbnya, I., Neo, T. K., & Korsunsky, A. M. (2019).

Investigations into the interface failure of yttria partially stabilised zirconia—Porcelain

dental prostheses through microscale residual stress and phase quantification. *Dental*

Materials, *35*(11), 1576–1593. https://doi.org/10.1016/j.dental.2019.08.098

Lunt, A., Terry, A., Ying, S., Baimpas, N., Sui, T., Kabra, S., Kelleher, J., King, S., Khin, N. T., &

Korsunsky, A. M. (2017). Characterisation of nanovoiding in dental porcelain using small

angle neutron scattering and transmission electron microscopy. *Dental Materials*, *33*(5),

486–497. https://doi.org/10.1016/j.dental.2017.02.005

Magnani, G., & Brillante, A. (2005). Effect of the composition and sintering process on mechanical

properties and residual stresses in zirconia–alumina composites. *Journal of the European*

Ceramic Society, *25*(15), 3383–3392. https://doi.org/10.1016/j.jeurceramsoc.2004.09.025

McMeeking, R. M., & Evans, A. G. (1982). Mechanics of Transformation-Toughening in Brittle

Materials. *Journal of the American Ceramic Society*, *65*(5), 242–246.

https://doi.org/10.1111/j.1151-2916.1982.tb10426.x

Mura, T. (1987). General theory of eigenstrains. In T. Mura (Ed.), *Micromechanics of defects in*

solids (pp. 1–73). Springer Netherlands. https://doi.org/10.1007/978-94-009-3489-4_1

Mura, T., & Koya, T. (1992). *Variational methods in mechanics*. Oxford university press New

York.

Ni, D. W., Olevsky, E., Esposito, V., Molla, T. T., Foghmoes, S. P. V., Bjørk, R., Frandsen, H. L.,

Aleksandrova, E., & Pryds, N. (2013). Sintering of Multilayered Porous Structures: Part II–

Experiments and Model Applications. *Journal of the American Ceramic Society*, *96*(8),

2666–2673. https://doi.org/10.1111/jace.12374

O'Brien, W. J. (2002). *Dental materials and their selection. Hanover Park (IL): Quintessence Pub.*

Co. Inc.

Olevsky, E., Molla, T. T., Frandsen, H. L., Bjørk, R., Esposito, V., Ni, D. W., Ilyina, A., & Pryds, N. (2013). Sintering of Multilayered Porous Structures: Part I-Constitutive Models. *Journal of the American Ceramic Society*, *96*(8), 2657–2665. https://doi.org/10.1111/jace.12375

Rinke, S., Gersdorff, N., Lange, K., & Roediger, M. (2013). Prospective evaluation of zirconia posterior fixed partial dentures: 7-year clinical results. *International Journal of Prosthodontics*, *26*(2).

Roediger, M., Gersdorff, N., Huels, A., & Rinke, S. (2010). Prospective evaluation of zirconia posterior fixed partial dentures: Four-year clinical results. *International Journal of Prosthodontics*, *23*(2).

Roehling, S., Schlegel, K. A., Woelfler, H., & Gahlert, M. (2019). Zirconia compared to titanium dental implants in preclinical studies—A systematic review and meta-analysis. *Clinical Oral Implants Research*, *30*(5), 365–395. https://doi.org/10.1111/clr.13425

Salvati, E., Lunt, A. J. G., Ying, S., Sui, T., Zhang, H. J., Heason, C., Baxter, G., & Korsunsky, A. M. (2017). Eigenstrain reconstruction of residual strains in an additively manufactured and shot peened nickel superalloy compressor blade. *Computer Methods in Applied Mechanics and Engineering*, *320*, 335–351. https://doi.org/10.1016/j.cma.2017.03.005

Salvati, Enrico, Sui, T., Lunt, A. J. G., & Korsunsky, A. M. (2016). The effect of eigenstrain induced by ion beam damage on the apparent strain relief in FIB-DIC residual stress evaluation. *Materials & Design*, *92*, 649–658. https://doi.org/10.1016/j.matdes.2015.12.015

Sato, T., Besshi, T., & Tada, Y. (1996). Effects of surface-finishing condition and annealing on transformation sensitivity of a 3 mol.% Y2O3 stabilized tetragonal zirconia surface under interaction of lubricant. *Wear*, *194*(1), 204–211. https://doi.org/10.1016/0043-1648(95)06867-8

Song, X., Liu, W. C., Belnoue, J. P., Dong, J., Wu, G. H., Ding, W. J., Kimber, S. A. J., Buslaps, T., Lunt, A. J. G., & Korsunsky, A. M. (2012). An eigenstrain-based finite element model and the evolution of shot peening residual stresses during fatigue of GW103 magnesium alloy.

International Journal of Fatigue, *42*, 284–295.
https://doi.org/10.1016/j.ijfatigue.2012.01.019

Song, Xiwen, Xie, M., Zhou, F., Jia, G., Hao, X., & An, S. (2011). High-temperature thermal
properties of yttria fully stabilized zirconia ceramics. *Journal of Rare Earths*, *29*(2), 155–
159. https://doi.org/10.1016/S1002-0721(10)60422-X

Stawarczyk, B., Özcan, M., Hallmann, L., Ender, A., Mehl, A., & Hämmerlet, C. H. F. (2013). The
effect of zirconia sintering temperature on flexural strength, grain size, and contrast ratio.
Clinical Oral Investigations, *17*(1), 269–274. https://doi.org/10.1007/s00784-012-0692-6

Swain, M. V. (2009). Unstable cracking (chipping) of veneering porcelain on all-ceramic dental
crowns and fixed partial dentures. *Acta Biomaterialia*, *5*(5), 1668–1677.
https://doi.org/10.1016/j.actbio.2008.12.016

Swain, M. V., Mercurio, V., Tibballs, J. E., & Tholey, M. (2019). Thermal induced deflection of a
porcelain–zirconia bilayer: Influence of cooling rate. *Dental Materials*, *35*(4), 574–584.
https://doi.org/10.1016/j.dental.2019.01.019

Takao, Y., Taya, M., & Chou, T. W. (1981). Stress Field Due to a Cylindrical Inclusion With
Constant Axial Eigenstrain in an Infinite Elastic Body. *Journal of Applied Mechanics*, *48*(4),
853–858. https://doi.org/10.1115/1.3157745

Timoshenko, S. (1925). Analysis of Bi-Metal Thermostats. *JOSA*, *11*(3), 233–255.
https://doi.org/10.1364/JOSA.11.000233

Tirry, W., & Schryvers, D. (2009). Linking a completely three-dimensional nanostrain to a
structural transformation eigenstrain. *Nature Materials*, *8*(9), 752–757.
https://doi.org/10.1038/nmat2488

Toraya, H., Yoshimura, M., & Somiya, S. (1984). Calibration curve for quantitative analysis of the
monoclinic-tetragonal ZrO2 system by X-ray diffraction. *Journal of the American Ceramic
Society*, *67*(6), C-119-C-121.

Turon-Vinas, M., & Anglada, M. (2018). Strength and fracture toughness of zirconia dental ceramics. *Dental Materials*, *34*(3), 365–375. https://doi.org/10.1016/j.dental.2017.12.007

Young, W. C., Budynas, R. G., & Roark, R. J. (2002). *Roark's Formulas for Stress and Strain*. McGraw-Hill.

Zhang, Y., Allahkarami, M., & Hanan, J. C. (2012). Measuring residual stress in ceramic zirconia–porcelain dental crowns by nanoindentation. *Journal of the Mechanical Behavior of Biomedical Materials*, *6*, 120–127. https://doi.org/10.1016/j.jmbbm.2011.11.006

Zhong, Z., & Meguid, S. A. (1996). On the Eigenstrain Problem of a Spherical Inclusion With an Imperfectly Bonded Interface. *Journal of Applied Mechanics*, *63*(4), 877–883. https://doi.org/10.1115/1.2787242